

leaning to steering hints that humans could similarly use a simple coupling between lean and lateral foot placement to aid balance. Furthermore, simulations used in the development of the Delft robot showed that the swift swing-leg motion not only increased fore-aft stability but also increased lateral stability. Indeed, the physical robot was not able to balance laterally without sufficient fore-aft swing-leg actuation. This highlights the possible coupling between lateral and sagittal balance in human walking.

The MIT biped shows that the efficiency of motor learning can be strongly influenced by the mechanical design of the walking system, both in robots and possibly in humans. Previous attempts at learning control for bipedal robots have required a prohibitively large number of learning trials in simulation (24) or a control policy with predefined motion primitives on the robot (25). By exploiting the natural stability of walking trajectories on the passive-dynamic walker, our robot was able to learn in just a few minutes without requiring any initial control knowledge. We also found that it was possible to estimate the walking performance gradient by making surprisingly small changes to the control parameters, allowing the robot to continue walking naturally as it learns. This result supports the use of actor-critic reinforcement learning algorithms as models for biological motor learning.

The conclusion that natural dynamics may largely govern locomotion patterns was already suggested by passive-dynamic machines. A common misconception has been that gravity power is essential to passive-dynamic walking, making it irrelevant to understanding human walking. The machines presented here demonstrate that there is nothing special about gravity as a power source; we achieve successful walking using small amounts of power added by ankle or hip actuation.

We expect that humanoid robots will be improved by further developing control of passive-dynamics-based robots and by paying closer attention to energy efficiency and natural dynamics in joint-controlled robots (26). Whatever the future of humanoid robots, the success of human mimicry demonstrated here suggests the importance of passive-dynamic concepts in understanding human walking.

References and Notes

1. D. A. Winter, *The Biomechanics and Motor Control of Human Gait* (Univ. of Waterloo Press, Waterloo, Ontario, Canada, 1987).
2. I. Kato *et al.*, *Proc. CISM-IFTOMM Theory and Practice of Robots and Manipulators* (Udine, Italy, 1973), pp. 12–24.
3. Y. Sakagami *et al.*, *Proc. IEEE/Robotics Society of Japan (RSJ) Int. Conf. Intell. Robots Syst.* (IEEE/RSJ, Lausanne, Switzerland, 2002), pp. 2478–2483.
4. C. Chevallereau *et al.*, *IEEE Control Syst. Mag.* **23**, 57 (2003).
5. F. Pfeiffer, K. Löffler, M. Gienger, *Proc. IEEE Int. Conf.*

- Robotics Automation* (IEEE, Washington, DC, 2002), pp. 3129–3135.
6. F. Zajac, *Crit. Rev. Biomed. Eng.* **17**, 359 (1989).
7. T. McGeer, *Int. J. Robotics Res.* **9**, 62 (1990).
8. S. H. Collins, M. Wisse, A. Ruina, *Int. J. Robot. Res.* **20**, 607 (2001).
9. Supporting online movies and text are available at Science Online.
10. Mechanical power is defined here as net positive mechanical work at the joints = $\int_0^T \sum [\omega_i M_i]^+ dt/T$ where T is the period of one step, ω_i is the relative angular velocity at one joint, M_i is the torque across that joint, $[x]^+ = x$ if $x > 0$ and 0 otherwise, and the sum is over all the joints. Because only the ankle does positive work on the Cornell robot, this can be measured by measuring the foot force as the ankle extends during push-off.
11. For the Cornell robot, total power was measured by averaging the voltage across a 1-ohm resistor put in series with the battery.
12. E. Atzler, R. Herbst, *Pflug. Arch. Gesamte Physiol.* **215**, 291 (1927).
13. N. H. Molen, R. H. Rozendal, W. Boon, *Proc. K. Ned. Akad. Wet. Ser. C* **75**, 305 (1972).
14. J. M. Donelan, R. Kram, A. D. Kuo, *J. Exp. Biol.* **205**, 3717 (2002).
15. Honda's ASIMO can walk at a variety of speeds, kick balls, and even climb stairs. It weighs 510 N, can walk at speeds up to 1.6 km hour⁻¹, and drains a 38.4-V, 10-A-hour battery in about 30 min (<http://world.honda.com/ASIMO/>). Using these numbers, we estimate $c_{et} \approx 3.2$ and, assuming a 50% drive train efficiency, $c_{mt} \approx 1.6$.
16. M. Wisse, J. van Frankenhuyzen, *Proc. Conf. Adaptive Motion Anim. Machines* (Kyoto, Japan, 2003).
17. M. Wisse, A. L. Schwab, R. Q. van der Linde, F. C. T. van der Helm, *IEEE Trans. Robot.*, in press.
18. R. Tedrake, T. W. Zhang, M. Fong, H. S. Seung, *Proc. IEEE/RSJ Int. Conf. Intell. Robots Syst.* (IEEE/RSJ, Sendai, Japan, 2004).
19. T. McGeer, *J. Theor. Biol.* **163**, 277 (1993).
20. H. Seung, *Neuron* **40**, 1063 (2003).

21. E. Todorov, *Nature Neurosci.* **5**, 1226 (2002).
22. A. D. Kuo, *J. Biomech. Eng.* **124**, 113 (2002).
23. A. Ruina, J. Bertram, M. Srinivasan, *J. Theor. Biol.*, in press.
24. H. Benbrahim, J. A. Franklin, *Robot. Auton. Syst.* **22**, 283 (1997).
25. A. Kun, W. T. Miller III, *Proc. IEEE Int. Conf. Robotics Automation* (IEEE, Minneapolis, MN, 1996).
26. J. Pratt, thesis, Massachusetts Institute of Technology (2000).
27. J. E. Wilson, U.S. Patent 2,140, 275; available at www.tam.cornell.edu/~ruina/hplab/.
28. R. Tedrake, T. W. Zhang, M. Fong, H. S. Seung, *Proc. IEEE Int. Conf. Robotics Automation* (IEEE, New Orleans, LA, 2004).
29. M. Garcia, A. Chatterjee, A. Ruina, *Dyn. Stab. Syst.* **15**, 75 (2000).
30. The Cornell robot was developed by S.C. with suggestions from A.R.; the Delft robot was developed by M.W. and J. van Frankenhuyzen on an Stichting Technische Wetenschappen grant, with help from A. Schwab; and the MIT robot was developed by R.T. and T. Weirui Zhang with help from M.-f. Fong and D. Tan in the lab of H. Sebastian Seung. A.R. and S.C. were funded by an NSF Biomechanics grant. R.T. was funded by the Packard Foundation and the NSF. The text was improved by comments from N. Agnihotri, C. Atkeson, J. Burns, A. Chatterjee, M. Coleman, J. Grizzle, P. Holmes, I. ten Kate, A. Kun, A. Kuo, Y. Loewenstein, S. van Nieuhuys, D. Paluska, A. Richardson, S. Seung, M. Srinivasan, S. Strogatz, and N. Sidor.

Supporting Online Material

www.sciencemag.org/cgi/content/full/307/5712/1082/DC1

Materials and Methods
SOM Text
Movies S1 to S3
References and Notes

22 November 2004; accepted 26 January 2005
10.1126/science.1107799

Terrestrial Gamma-Ray Flashes Observed up to 20 MeV

David M. Smith,^{1*} Liliana I. Lopez,² R. P. Lin,³ Christopher P. Barrington-Leigh⁴

Terrestrial gamma-ray flashes (TGFs) from Earth's upper atmosphere have been detected with the Reuven Ramaty High Energy Solar Spectroscopic Imager (RHESSI) satellite. The gamma-ray spectra typically extend up to 10 to 20 megaelectron volts (MeV); a simple bremsstrahlung model suggests that most of the electrons that produce the gamma rays have energies on the order of 20 to 40 MeV. RHESSI detects 10 to 20 TGFs per month, corresponding to ~50 per day globally, perhaps many more if they are beamed. Both the frequency of occurrence and maximum photon energy are more than an order of magnitude higher than previously known for these events.

Terrestrial gamma-ray flashes (TGFs) were unexpectedly detected from Earth's atmosphere by the Burst and Transient Source Experiment

(BATSE) on the Compton Gamma-Ray Observatory (CGRO), a NASA satellite in low-Earth orbit between 1991 and 2000. Each BATSE TGF (I) lasted between a fraction of a millisecond and several milliseconds, shorter than all other transient gamma-ray phenomena observed from space. Since they were first detected, it has also been noticed that TGFs had a harder energy spectrum (higher average energy per photon) than any of these other phenomena (I).

Fishman *et al.* (I) immediately interpreted the TGFs as high-altitude electrical discharges and found a correlation with thunderstorms.

¹Physics Department and Santa Cruz Institute for Particle Physics, University of California, Santa Cruz, 1156 High Street, Santa Cruz, CA 95064, USA.

²Astronomy Department and Space Sciences Laboratory, University of California, Berkeley, Berkeley, CA 94720, USA. ³Physics Department and Space Sciences Laboratory, University of California, Berkeley, Berkeley, CA 94720, USA. ⁴University of British Columbia, 2329 West Mall Vancouver, BC V6T 1Z4 Canada.

*To whom correspondence should be addressed. E-mail: dsmith@scipp.ucsc.edu

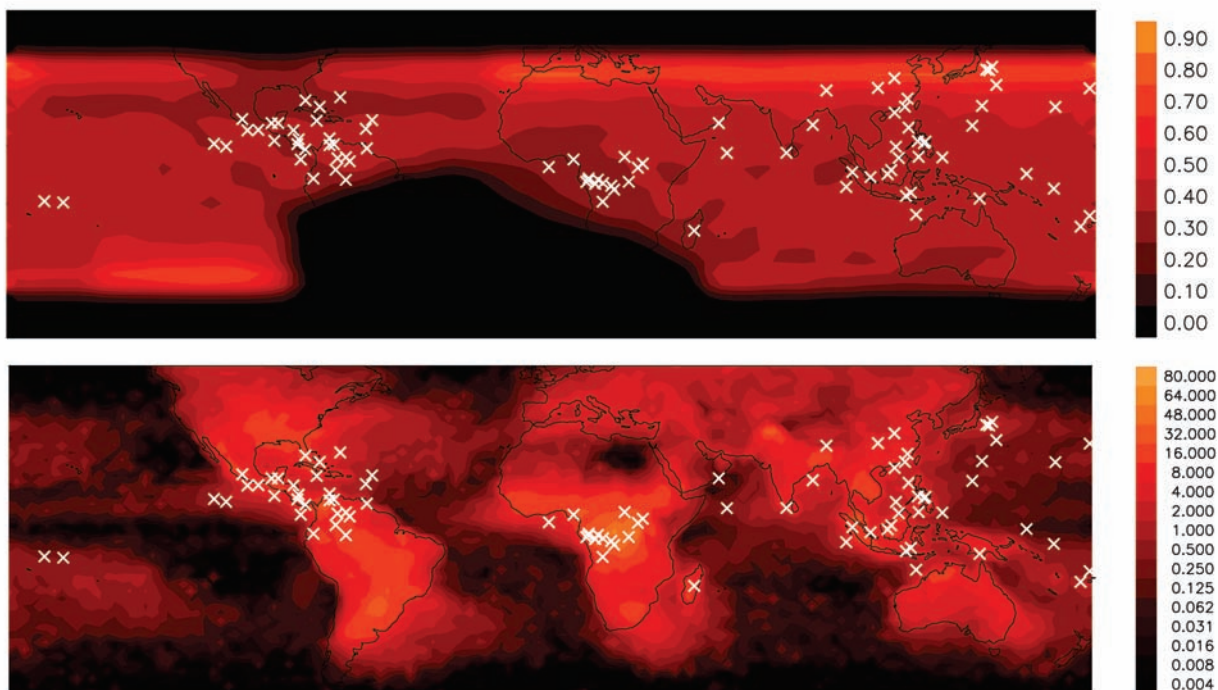


Fig. 1. RHESSI position during each recorded TGF, plotted over (i) the expected distribution of observed TGFs if the population were evenly distributed over the globe, with the scale in fraction of maximum exposure (**top**); and (ii) long-term lightning frequency data (29), with the scale in flashes per square kilometer per year (**bottom**).

Hard x-rays and/or gamma rays have also been detected in thunderclouds and at ground level from natural and triggered lightning strokes (2–5). Acceleration of electrons to high energies in electric fields above thunderstorms was predicted in 1925 by Wilson (6), and this runaway process was recently shown (7) to be capable of avalanche multiplication, making its variants (8–10) good candidates for the TGF parent process.

Runaway breakdown is one of several candidate mechanisms for the production of red sprites and blue jets, transient luminous events (TLEs) in the upper atmosphere above thunderstorms (11). The production of upward-going, relativistic electrons, necessary for TGFs, is not necessary for sprites, a few of which have been observed in high-altitude electric fields of the opposite polarity (12); other sorts of breakdown such as streamer formation (13) may be at work in sprites. There is no direct evidence linking TGFs to any of the family of TLEs. In 1996, Inan *et al.* (14) reported a burst of radio noise (“sferic”), typical of lightning, at Palmer Station, Antarctica, from the direction of CGRO’s position during one of the BATSE TGFs. This sferic showed positive cloud-to-ground polarity and a slow tail, features typical of sprite-producing lightning. Recently, sferics were seen with five out of six additional BATSE TGFs for which data were available at Palmer (15).

The high-energy electron beams that cause TGFs may also produce some secondary phenomena if they escape the atmosphere and

travel along field lines in the magnetosphere: They may interact in the magnetically conjugate point of Earth’s atmosphere (16), may populate the inner radiation belt (17), and may be directly detectable from satellites.

BATSE recorded somewhat less than one TGF per month, when a trigger criterion was met on board (1) that initiated data collection at high time resolution in four energy channels, the highest of which collected all pulses above 300 keV. The spectra were consistent with power laws having photon indices between -0.6 and -1.5 (18). Interpreted as bremsstrahlung, this result suggested electron energies of ~ 1 MeV or higher, but could not distinguish between that and much higher energies; only by observing the cutoff of the bremsstrahlung at high energies can the maximum electron energy be determined.

The Reuven Ramaty High Energy Solar Spectroscopic Imager (RHESSI) (19) is a NASA Small Explorer spacecraft designed to study x-rays and gamma rays from solar flares. It was launched on 5 February 2002, into an orbit of inclination 38° and of altitude 600 km, which covers most of Earth’s thunderstorm zones and reaches geomagnetic latitudes up to $\sim 50^\circ$. RHESSI’s germanium detectors (20) detect photons from any direction in the sky and record each photon individually, so that no on-board trigger is necessary.

We present 86 TGFs from 6 months of RHESSI data, two near the beginning of the mission (April and May 2002) and four recent (July to October 2004). Data are available

from the entire mission, and the analysis is ongoing. The RHESSI TGFs range from 0.2 to 3.5 ms in duration and contain from 17 to 101 detected photons. Sometimes two RHESSI flashes are detected from a single geographic region, either during one satellite pass (in one case 15 s apart) or separated by a full spacecraft orbit (about 96 min). These clusters suggest activity from a single storm.

Figure 1 shows the position of RHESSI during each of the TGFs. The color scale in the top plot is the product of the time spent above each position and the sensitivity to TGFs at those times, giving the number of TGFs expected at each position if they were uniformly distributed on the globe. When the spacecraft passes through Earth’s inner radiation belt at the South Atlantic Anomaly, no data are taken. RHESSI’s TGFs, like BATSE’s, congregate where lightning (bottom plot) is common; note the region of central Africa that has the highest rate of lightning and the tightest cluster of RHESSI TGFs. There is a notable lack of TGFs in the southern United States, where RHESSI’s magnetic latitude is highest and there is a lot of lightning, despite theoretical expectations that it should be easier to accelerate electrons upwards at high altitudes when Earth’s magnetic field is further from horizontal (21, 22). With only 6 months of data, however, it is premature to declare that TGFs do not occur in this region.

With its high energy resolution and broad energy range, RHESSI is able to study the spectra of TGFs in detail. Figure 2, left panel,

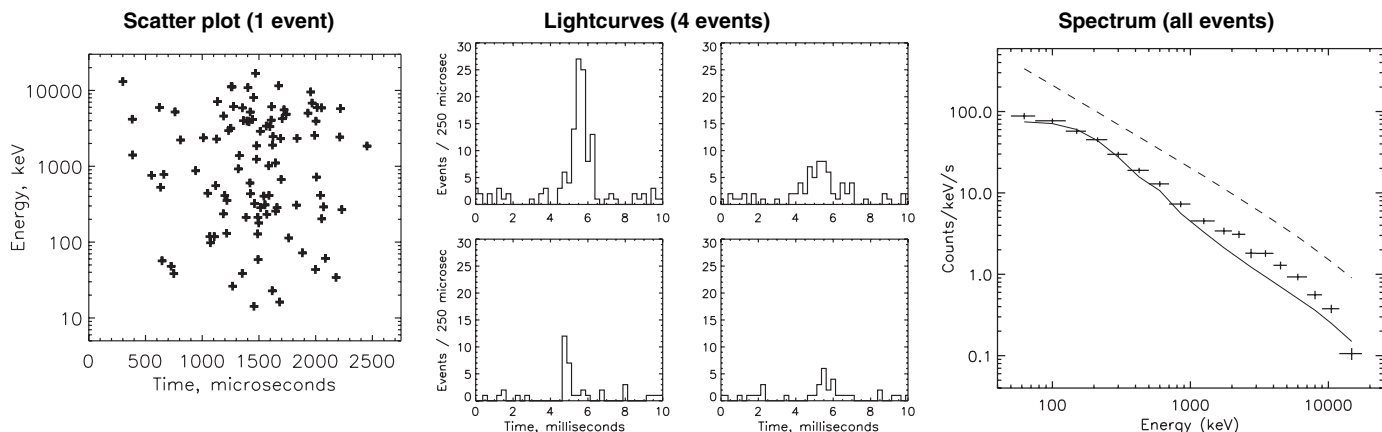


Fig. 2. (Left) Scatter plot of energy versus time for the brightest RHESSI TGF. (Center) Histograms of count rate versus time for the brightest, longest, faintest, and shortest (clockwise from upper left). RHESSI TGF

detected so far. (Right) Summed energy spectrum of all the RHESSI TGFs, shown with the expected instrumental response (solid curve) to isotropic thin-target bremsstrahlung from 35 MeV electrons (dashed line).

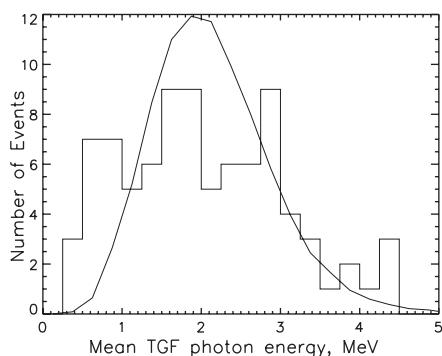


Fig. 3. Distribution of average energy for the RHESSI TGFs (histogram) along with a simulation assuming that each TGF has exactly the spectrum shown in Fig. 2.

shows count energies versus arrival time for the largest TGF. The center panels show four representative lightcurves, and the right panel shows the summed energy spectrum of the whole population. The background gamma-ray spectrum has been subtracted.

The position of the high-energy cutoff suggests that the energy of the electrons responsible for the bulk of the bremsstrahlung is on the order of 20 to 40 MeV. The spectrum is reminiscent of that seen once at ground level by Dwyer *et al.* (5) from triggered lightning. The right panel of Fig. 2 also shows the expected signal from isotropic, thin-target bremsstrahlung of 35-MeV monoenergetic electrons. This is not, of course, a realistic model, but it demonstrates that the correct electron spectrum will be extremely hard. The dashed curve is the model spectrum itself, and the solid curve is its convolution with the instrumental response for comparison with the data. An unmodeled excess at several MeV is apparent, which is expected for beamed TGFs viewed along the beam axis, due to the peaking of the bremsstrahlung cross section at high energies and small angles (23).

The flattening of the spectrum below 200 keV is consistent with absorption in mate-

rials surrounding the detectors. The BATSE data down to 25 keV were consistent with a power law when corrected for the instrumental response (18). These results suggest that TGFs occur relatively high in the atmosphere and are probably not from the same source that produces gamma rays seen on the ground (4, 5). Assuming that the intrinsic TGF spectrum does not rise suddenly just where the atmospheric cross sections rise below 100 keV, and assuming that all the photons come from a single altitude, we can constrain that altitude to be >25 km by noting that the lowest RHESSI energy point shown (about 60 keV) does not have an extra e -folding of absorption compared to the points at several hundred keV. Monte Carlo simulations of electron and gamma-ray propagation in the atmosphere will produce stronger altitude constraints and address other scenarios that might fit the data, such as a hard electron spectrum below 25 km combined with a softer spectrum at higher altitudes. Future orbiting detectors sensitive to lower energies (~ 10 keV) would give even better constraints, due to the much higher cross sections for atmospheric absorption at lower energies.

The TGFs that make up the composite spectrum may have different spectra (18). Although each TGF has too few photons for a good spectral fit, the mean photon energy for each TGF can be compared (Fig. 3). The smooth curve is a larger set of artificial TGFs, each one having the mean spectrum in Fig. 2 and the same number of counts as one randomly selected real TGF. The width of this curve indicates that some, but not all, of the spectral variation we see is due to the small number of photons per TGF. Nemiroff *et al.* (18) and Feng *et al.* (24) found that BATSE TGF spectra evolved from hard to soft within each flash, and that the bursts were somewhat longer at low energies. We see both effects in the RHESSI flashes, but at a low level; more detailed analyses will be forthcoming.

Individual photons greater than 10 MeV appear in 60 of the 86 TGFs. Summing all the TGFs, we find 47 photon events that exceed one detector's threshold of ~ 18 MeV and 9 photon events that, because they deposited energy in more than one detector, we can be certain were above 20 MeV. The expected values of these numbers at normal background rates would be 16.5 and 2.8 photon events, respectively. The electron accelerator responsible for TGFs may thus work to higher energies than any other natural accelerator in Earth's atmosphere or magnetosphere. If the acceleration is by a DC electric field, it requires a potential drop of at least 30 MV (higher when taking frictional energy losses into account). This is comparable to predicted potentials between cloudtops and the ionosphere (25).

To estimate the global average rate of TGFs, we need RHESSI's footprint for TGF detection. Although RHESSI has a line of sight to the horizon at 2700 km, only an extremely bright flash at that distance would be detected above background. Assuming that TGFs are isotropic emitters and equally luminous, and considering the dynamic range of our events, we estimate an effective footprint of radius ~ 1000 km. Then the observed TGF rate of 86 events in 183 days corresponds to ~ 50 events per day summed over the latitudes RHESSI covers. Upward beaming of the photons would reduce the radius of detectability. One model predicted a ~ 100 -km beam (21), in which case the true global rate could be two orders of magnitude higher. Even 5000 TGFs per day is only 0.1% of the global lightning rate, which the space-based Optical Transient Detector recently measured to be 44 ± 5 per second (26). We cannot rule out an even larger population of TGFs below RHESSI's detection threshold.

The average number of relativistic electrons in each flash can be estimated. Assuming monoenergetic 35-MeV electrons (Fig. 2), an average photon energy of 2.5 MeV, thick-target bremsstrahlung, isotropic emission, a distance

of 600 km to the source, total bremsstrahlung production efficiency of 13% (27), 30 photons detected for an average TGF, and an instrumental effective area of 250 cm², we require $\sim 3 \times 10^{15}$ 35-MeV electrons, for a total energy of ~ 20 kJ or a power of ~ 40 MW over 0.5 ms. Beaming would make these numbers lower, even as it made the inferred number of TGFs higher. Although thin-target bremsstrahlung gives a better fit, the electron content in the thin-target case is unconstrained and could be much higher. For upward-beamed electrons, ignoring Earth's magnetic field, the transition between thin and thick target would take place at ~ 30 km.

TGFs near geomagnetic latitude 45° have been considered as a source of ~ 1 -MeV electrons in Earth's inner radiation belt by Lehtinen *et al.* (17). Inner-belt electrons above 10 MeV are more relevant to our results and were detected by Mariya-2 on the Mir station (28). The RHESSI TGFs, however, have an average geomagnetic latitude of 14°, and for these the electrons would be tied to magnetic field lines that skim the atmosphere and could not become trapped. As we analyze the whole RHESSI data set—almost 3 years and counting—we will either measure or place limits on high-latitude TGFs that may contribute to the inner-belt electrons above 10 MeV.

We are searching with a number of groups for coincidences between RHESSI TGFs and different kinds of lightning and TLEs. With TGFs for the whole RHESSI mission, we will compare these populations statistically as well.

References and Notes

1. G. J. Fishman *et al.*, *Science* **264**, 1313 (1994).
2. G. K. Parks, B. H. Mauk, R. Spiger, J. Chin, *Geophys. Res. Lett.* **8**, 1176 (1981).
3. K. B. Eack, W. H. Beasley, W. D. Rust, T. C. Marshall, M. Stolzenburg, *Geophys. Res. Lett.* **23**, 2915 (1996).
4. C. B. Moore, K. B. Eack, G. D. Aulich, W. Rison, *Geophys. Res. Lett.* **28**, 2141 (2001).
5. J. R. Dwyer *et al.*, *Geophys. Res. Lett.* **31**, L05119 (2004).
6. C. T. R. Wilson, *Proc. Phys. Soc. London* **37**, 32D (1925).
7. A. V. Gurevich, G. M. Milikh, R. Roussel-Dupré, *Phys. Lett. A* **165**, 463 (1992).
8. R. Roussel-Dupré, E. Symbalysti, Y. Taranenko, V. Yukhimuk, *J. Atmos. Sol. Terr. Phys.* **60**, 917 (1998).
9. G. M. Milikh, J. A. Valdivia, *Geophys. Res. Lett.* **26**, 525 (1999).
10. A. V. Gurevich, G. M. Milikh, *Phys. Lett. A* **262**, 457 (1999).
11. For a review of TLEs, see T. Neubert, *Science* **300**, 747 (2003).
12. C. P. Barrington-Leigh, U. S. Inan, M. Stanley, S. A. Cummer, *Geophys. Res. Lett.* **26**, 3605 (1999).
13. V. P. Pasko, U. S. Inan, T. F. Bell, *Geophys. Res. Lett.* **25**, 2123 (1998).
14. U. S. Inan, S. C. Reising, G. J. Fishman, J. M. Horack, *Geophys. Res. Lett.* **23**, 1017 (1996).
15. U. S. Inan, personal communication.
16. N. G. Lehtinen, U. S. Inan, T. F. Bell, *J. Geophys. Res.* **106**, 28841 (2001).

17. N. G. Lehtinen, U. S. Inan, T. F. Bell, *Geophys. Res. Lett.* **27**, 1095 (2000).
18. R. Nemiroff, J. T. Bonnelli, J. P. Norris, *J. Geophys. Res.* **102**, 9659 (1997).
19. R. P. Lin *et al.*, *Solar Phys.* **210**, 1 (2002).
20. Materials and methods are available as supporting material on Science Online.
21. N. G. Lehtinen, T. F. Bell, U. S. Inan, *J. Geophys. Res.* **104**, 24699 (1999).
22. L. P. Babich, R. I. Il'kayev, A. Yu. Kudryavtsev, I. M. Kutsyk, R. A. Roussel-Dupré, *Dokl. Earth Sci.* **381**, 994 (2001).
23. R. Roussel-Dupré, personal communication.
24. H. Feng, T. P. Li, M. Wu, M. Zha, Q. Q. Zhu, *Geophys. Res. Lett.* **29**, 1036 (2002).
25. P. T. Tonev, P. I. Y. Velinov, *Adv. Space Res.* **31**, 1443 (2003).
26. H. J. Christian *et al.*, *J. Geophys. Res.* **108**, 4005 (2003).
27. H. W. Koch, J. W. Motz, *Rev. Mod. Phys.* **31**, 920 (1959).
28. A. M. Galper *et al.*, *J. Geophys. Res.* **104**, 28685 (1999).
29. The v1.0 gridded satellite lightning data were produced by the NASA Lightning Imaging Sensor/Optical Transient Detector Science Team (Principal Investigator, H. J. Christian, NASA/Marshall Space Flight Center) and are available from the Global Hydrology Resource Center (<http://ghrc.msfc.nasa.gov>).
30. We thank R. Roussel-Dupré, S. Mende, S. Frey, U. Inan, S. A. Cummer, Y. Zhai, C. J. Rodger, Y. Yair, Y. Takahashi, and D. Fargion for helpful discussions and NASA for supporting this work under contract NAS5-98033.

Supporting Online Material

www.sciencemag.org/cgi/content/full/307/5712/1085/DC1

Materials and Methods
References and Notes

12 November 2004; accepted 31 December 2004
10.1126/science.1107466

Iron Isotope Constraints on the Archean and Paleoproterozoic Ocean Redox State

Olivier J. Rouxel,^{1*} Andrey Bekker,² Katrina J. Edwards¹

The response of the ocean redox state to the rise of atmospheric oxygen about 2.3 billion years ago (Ga) is a matter of controversy. Here we provide iron isotope evidence that the change in the ocean iron cycle occurred at the same time as the change in the atmospheric redox state. Variable and negative iron isotope values in pyrites older than about 2.3 Ga suggest that an iron-rich global ocean was strongly affected by the deposition of iron oxides. Between 2.3 and 1.8 Ga, positive iron isotope values of pyrite likely reflect an increase in the precipitation of iron sulfides relative to iron oxides in a redox stratified ocean.

The rise of atmospheric oxygen, which began by about 2.3 Ga (1–3), was one of the most important changes in Earth's history. Because Fe, along with C and S, are linked to and maintain the redox state of the surface environment, the concentration and isotopic composition of Fe in seawater were likely affected by the

change in the redox state of the atmosphere. The rise of atmospheric oxygen should have also led to dramatic changes in the ocean Fe cycle because of the high reactivity of Fe with oxygen. However, deposition of banded iron formations (BIFs) during the Paleoproterozoic era suggests that the deep ocean remained anoxic, at least episodically, until about 1.8 Ga, which allowed high concentrations of Fe(II) to accumulate in the deep waters (4).

Here we use Fe isotope systematics (5) to provide constraints on the redox state of the Archean and Paleoproterozoic oceans and to identify direct links between the oxidation of the atmosphere and the Fe ocean cycle.

Laboratory and field studies suggest that Fe isotope variations are associated mainly with redox changes (6, 7). Lithogenic sources of Fe on the modern oxygenated Earth, such as weathering products, continental sediments, river loads, and marine sediments, have isotopic compositions similar to those of igneous rocks (8, 9). In contrast, seafloor hydrothermal sulfides and secondary Fe-bearing minerals from the altered oceanic crust span nearly the entire measured range of $\delta^{56}\text{Fe}$ values (5) on Earth, from -2.1 to 1.3 per mil (‰) (10, 11). Large variations of $\delta^{56}\text{Fe}$ (from -2.5 to 1.0 ‰) in Late Archean to Early Paleoproterozoic BIFs have been also reported (12), which highlight the roles of ferrous Fe oxidation, fluid-mineral isotope fractionation, and potentially microbial processes in the fractionation of Fe isotopes.

Study of S isotope composition of sedimentary pyrite over geological time has placed important constraints on the S cycle and the evolution of ocean chemistry (13). Here we apply a similar time-record approach in order to explore potential changes in Fe isotope compositions. Pyrite formation in modern organic-rich marine sediments is mediated by sulfate-reducing bacteria and proceeds essentially through the dissolution and reduction of lithogenic Fe oxides and Fe silicates to Fe(II), either below the sediment-water interface or in stratified euxinic bottom waters (14–16). During reduction of Fe oxides, diagenetic fluids with isotopically light Fe(II) may be produced (17, 18). However, the Fe

¹Marine Chemistry and Geochemistry Department, Geomicrobiology Group, Woods Hole Oceanographic Institution, Mail Stop 8, Woods Hole, MA 02543, USA. ²Geophysical Laboratory, Carnegie Institution of Washington, 5251 Broad Branch Road NW, Washington, DC 20015, USA.

*To whom correspondence should be addressed. E-mail: orouxel@whoi.edu